Simulation of the Direct Radiative Effect of Mineral Dust Aerosol on the Climate at the Last Glacial Maximum

XU YUE* AND HUIJUN WANG

CCRC, and NZC, IAP, CAS, Beijing, China

HONG LIAO

LAPC, IAP, and CCRC, CAS, Beijing, China

DABANG JIANG

NZC, IAP, and Key Laboratory of Regional Climate–Environment Research for Temperate East Asia, and CCRC, CAS, Beijing, China

(Manuscript received 5 May 2010, in final form 28 August 2010)

ABSTRACT

The climatic responses to the direct radiative effect of dust aerosol at the Last Glacial Maximum (LGM) are examined using a general circulation model with online simulation of dust. The predicted global dust emission at the LGM is 2.3 times as large as the present-day value, which is the combined effect of the expansion of dust sources and the favorable meteorological parameters (MPs; e.g., the strong surface wind and the low air humidity) under the LGM climate. Simulated global dust emission is 1966 Tg yr^{-1} with present-day dust sources and MPs, 2820 Tg yr^{-1} with LGM dust sources and current MPs, 2599 Tg yr^{-1} with present-day dust sources and LGM MPs, and 4579 Tg yr^{-1} with LGM sources and MPs. The simulated percentage increases of dust concentrations are the largest at high latitudes in both hemispheres, which are consistent with the deposition data from geological records. The LGM dust is estimated to exert global annual-mean shortwave (SW) and longwave (LW) radiative forcing (RF) of -4.69 and $+1.70$ W m^{-2} at the surface, respectively, and -0.58 and $+0.68$ W m^{-2} at the top of the atmosphere, respectively. On a global- and annual-mean basis, surface air temperature (SAT) is predicted to be reduced by 0.18 K and precipitation is reduced by 0.06 mm day^{-1}, as a result of the net (SW and LW) radiative effect of dust at the LGM. Two sensitivity studies are performed to identify the uncertainties in simulated climatic effect of LGM dust that arise from the assumed LW and/or SW absorption by dust: 1) in the absence of dust LW radiative effect, the LGM global- and annual-mean SAT is predicted to be further reduced by 0.19 K; and 2) when the single scattering albedo of the Saharan dust at 0.55 μm is increased from 0.89 to 0.98 in the LGM climate simulation, the LGM dust-induced annual- and global-mean surface cooling increases from 0.18 to 0.63 K even with both SW and LW radiative effects of dust. In these two sensitivity studies, the LGM dust is predicted to induce an average cooling of 0.42 and 0.72 K in SAT, respectively, over the tropical oceans.

1. Introduction

Mineral dust aerosol plays important and multiple roles in the earth system. It can absorb and scatter both shortwave (SW) and longwave (LW) radiation (Carlson and Benjamin 1980; Miller and Tegen 1998), influence optical property and lifetime of clouds (Sassen 2002; Lohmann and Diehl 2006), change surface albedo by deposition on ice and snow (Peltier and Marshall 1995; Krinner et al. 2006; Painter et al. 2007), and fertilize phytoplankton by oceanic deposition (Prospero et al. 1996; Watson et al. 2000). These physical and biochemical processes exert impacts on energy balance and cycles of atmospheric components (such as water vapor and CO_2).

The Last Glacial Maximum (LGM; about 21 000 yr ago) is the most recent glacial period with an extremely

* Current affiliation: School of Engineering and Applied Sciences, Harvard University, Cambridge, Massachusetts.

Corresponding author address: Prof. Huijun Wang, NZC, Institute of Atmospheric Physics, Chinese Academy of Sciences, P.O. Box 9804, Beijing 100029, China.
E-mail: wanghj@mail.iap.ac.cn

DOI: 10.1175/2010JCLI3827.1

cold, dry, and dusty climate. Compared to present day, the annual-mean LGM surface temperature from the proxy data was lower by 2–5 K over the tropical oceans (Guilderson et al. 1994; Patrick and Thunell 1997; Wolff et al. 1998; Ballantyne et al. 2005). Most coupled climate models, by taking into consideration the changes in orbital parameters, continental ice sheet, topography, coastline, and concentrations of greenhouse gases, obtained only a cooling of 1.7–2.4 K in tropical regions (Jansen et al. 2007 and references therein).

Since atmospheric dust loadings during cold periods are generally much higher than those during warm periods (Petit et al. 1990), several studies have investigated the contribution of high concentrations of dust aerosol to the cooling at the LGM. Earlier simulations of mineral dust aerosol in the LGM climate did not account for the changes in land surface type and hence could not reproduce the high dust concentrations at the LGM (e.g., Genthon 1992; Joussaume 1993; Andersen et al. 1998). Some recent studies considered the changes in dust sources by using the simulated LGM land cover from vegetation models (e.g., Mahowald et al. 1999; Lunt and Valdes 2002; Werner et al. 2002; Mahowald et al. 2006a; Takemura et al. 2009), and results from these simulations reported an increase of 1.5–3 times in global dust emission at the LGM relative to present day. Using the simulated LGM dust fields from Mahowald et al. (1999), Claquin et al. (2003) estimated that the global-mean LGM dust radiative forcing (RF) at the top of the atmosphere (TOA) was -3.2 W m^{-2}, which was larger than the RF of -1.2 W m^{-2} by present-day dust. Mahowald et al. (2006b) obtained a TOA dust RF of -1.0 W m^{-2} during the LGM by using a different climate model. Recently, Takemura et al. (2009) found that the tropopause direct RF of dust at the LGM was close to 0 W m^{-2} because the positive forcings over bright desert and ice surfaces offset the negative forcings over dark oceans.

There have been large uncertainties in estimating the climate responses to dust RF during the glacial period. Harvey (1988) showed that a plausible increase in aerosol (including dust and sea salt) optical depth during the LGM could have caused a further global-mean cooling of 2°–3°C. Mahowald et al. (2006b) used the National Center for Atmospheric Research (NCAR)'s Community Climate System Model, version 3 (CCSM3) and predicted that dust aerosol led to a global-mean cooling of 0.85 K at the LGM, with a maximum cooling exceeding 2 K at high latitudes in the Northern Hemisphere (NH). The cooling induced by dust aerosol at the LGM helps to reduce the model biases of underestimating the cooling during the LGM (Kohfeld and Harrison 2000; Schneider et al. 2006). Overpeck et al. (1996), however, found that the high dust loading at the LGM caused a significant regional warming of more than 5 K over the downwind regions of Asian and ice-marginal dust sources.

The large deviations in climate responses among different studies can be attributed to the differences in consideration of the radiative effect of dust aerosol. For example, Harvey (1988) and Bar-Or et al. (2008) did not consider LW absorption by dust in their simulations and obtained a strong cooling during the LGM. In simulations by Harvey (1988), Claquin et al. (2003), and Mahowald et al. (2006b), the values of single-scattering albedo (SSA) of dust aerosol were set to be 0.94 (at solar spectra ranging from 0.3 to 0.9 μm), 0.97 (at 0.64 μm), and 0.95 (at 0.50 μm), respectively, leading to a weak SW absorption and hence a strong cooling by dust in these studies. Observations have shown that the SSA of pure dust particles at the wavelength of 0.67 μm can range from 0.90 to 0.99 (Forster et al. 2007), suggesting that the SW absorption of dust aerosol could be stronger than that estimated in previous LGM studies.

Other factors that contribute to the uncertainties in simulated climatic effects of LGM dust are the two-way dust cycle–climate coupling and the sea surface temperature (SST) responses to dust forcing. Yue et al. (2010) showed that simulations with an interactive dust cycle predict a stronger cooling than those using the prescribed dust concentrations. The dust-induced reductions in SST lead to the reduction in precipitation (or wet deposition of dust), which increases the global burden of small dust particles and consequently enhances the cooling by dust at the surface. Mahowald et al. (2006b) investigated the dust-induced global-mean temperature responses at the LGM with the two-way dust cycle–climate coupling, but they did not examine the spatial pattern of the climate responses.

Here we use the general circulation model IAP9L-AGCM with the two-way dust cycle–climate coupling to 1) simulate and evaluate the dust climatology at the LGM, 2) examine the spatial patterns of the LGM climate responses to dust LW and SW forcings, and 3) examine the sensitivity of the LGM temperature responses to dust SSA and the consideration of LW RF. This builds on our previous work, in which the equilibrium terrestrial biosphere model BIOME3 (Haxeltine and Prentice 1996) was driven by the nine-level AGCM developed by the Institute of Atmospheric Physics IAP9L-AGCM to obtain the LGM vegetation (Jiang 2008), a Global Transport Model of Dust (GMOD) was coupled into the IAP9L-AGCM to simulate dust–climate interactions (Yue et al. 2009, 2010), and the radiative scheme in IAP9L-AGCM was updated to consider both the SW and LW radiative effects of dust aerosol (Yue et al. 2010).

The description of model and numerical experiments are presented in the next section. In section 3, the

simulated LGM dust climatology is presented and evaluated with the proxy data. Sections 4 and 5 examine the RF and climatic effects of the LGM dust, respectively. The sensitivity of the simulated LGM temperature responses to the consideration of dust SW and LW absorption is discussed in section 6.

2. The model and numerical experiments

a. The IAP9L-AGCM

The general circulation model utilized in this study is the IAP9L-AGCM (Zeng et al. 1989; Zhang 1990; Liang 1996). It has a horizontal resolution of 4° × 5° in latitude and longitude and has nine vertical levels. The model is coupled with a mixed layer ocean model (Hansen et al. 1984) that utilizes an annual-mean mixed layer depth derived from Levitus et al. (2000). The radiative scheme in the IAP9L-AGCM follows that from the NCAR Community Climate Model 3 (CCM3) (Yue and Wang 2009). This version of the GCM has been used in a number of paleoclimate studies (e.g., Wang 1999, 2002; Jiang et al. 2003, 2005; Ju et al. 2007; Zhang et al. 2007a,b; Jiang 2008).

b. The online simulation of mineral dust in the IAP9L-AGCM

Dust simulation (the GMOD) was integrated into the IAP9L-AGCM by Yue et al. (2009). The dust scheme simulates four dust bins with radii ranging from 0.1 to 10.0 μm. The emission scheme was taken from Wang et al. (2000):

$$Q_p = \begin{cases} C_1 C_2 s_p u_*^2 \left(1 - \dfrac{u_{*_t}}{u_*}\right)\left(1 - \dfrac{\mathrm{RH}}{\mathrm{RH}_t}\right) & u_* \geq u_{*_t} \text{ and } \mathrm{RH} \leq \mathrm{RH}_t \\ 0 & \text{otherwise} \end{cases}, \tag{1}$$

where Q_p is the uplift flux of particle size class p; C_2 is an empirical constant; and C_1 is the potential emission coefficient of the soil, which is determined based on the land surface types in the GCM. Desert, scrubland, and short grassland are allowed to have dust mobilization; the emissions from these three types of surfaces are assumed to have a ratio of 10:3:1 to reflect different capabilities in dust mobilization. In addition, no dust emissions are allowed over grid boxes that are covered by ice or snow when snow depth is more than 0.02 m. Also, s_p represents the fraction of dust mass in size bin p to total dust mass emitted, and u_{*t} and RH_t are the threshold values for friction velocity and relative humidity at the surface, respectively; dust particles can be blown into the atmosphere only when the surface wind speed u_* exceeds u_{*t} and relative humidity RH is smaller than RH_t. The utility of RH as a constraint for dust uplift instead of soil moisture is a unique feature of the dust simulation (Yue et al. 2009). Observations show that RH at the surface is closely correlated with soil moisture, including both spatial pattern and temporal variation. Dry deposition of dust is determined by the settling velocity, which considers the effects of both gravity and turbulence (Yue et al. 2009). The wet scavenging of dust is proportional to the precipitation rate, with size-dependent coefficients (Yue et al. 2009). Yue et al. (2009) evaluated the dust model GMOD with several sets of observations. The GMOD reproduces reasonably well dust concentrations at 18 sites [mean bias (MB) of -0.67 μg m^{-3}, normalized mean bias (NMB) of -8.0%], aerosol optical thickness at 16 sites (MB of -0.04, NMB of -26.7%), and deposition of dust at 251 sites with a logarithmic correlation coefficient of 0.84 between simulated and observed deposition.

c. Simulation of the radiative effects of dust

The radiative transfer scheme in the IAP9L-AGCM utilizes a δ-Eddington approximation with 18 spectral intervals ranging from 0.2 to 5.0 μm (Briegleb 1992) to calculate the SW radiation at each model hour. At the LW spectra, the GCM parameterizes the absorptivity/emissivity of water vapor, carbon dioxide, ozone, and trace gases (Ramanathan and Downey 1986). The original radiative scheme has been updated to consider the radiative effects of dust (Yue et al. 2010). For the SW effect of dust, we calculate dust extinction coefficients, SSA, and asymmetry factors using the Mie theory (de Rooij and van der Stap 1984; Mishchenko et al. 1999). The refractive indices of dust are taken from Woodward (2001), which are wavelength-dependent values complied based on measurements at different locations. For the LW effect of dust, we employ the exponential transmission approximation proposed by Carlson and Benjamin (1980). The simulated dust transmission is then multiplied by the atmospheric transmission to represent the LW perturbation by dust (Yue et al. 2010).

d. Simulation of the LGM climate and vegetation

For the simulation of the LGM climate, the earth's orbital parameters are recalculated using the equations in Berger (1978). The atmospheric CO_2 concentration at the LGM is set to 200 ppmv (e.g., Barnola et al. 1987). The LGM continental ice sheet, topography, and coastline are implemented into the GCM using the datasets compiled by Peltier (2004). The Peltier datasets have a horizontal resolution of 1° × 1° on a global scale and are used in this work after merging values in twenty 1° × 1° grid cells into one 4° × 5° grid box of our GCM. Ice sheet is defined if at

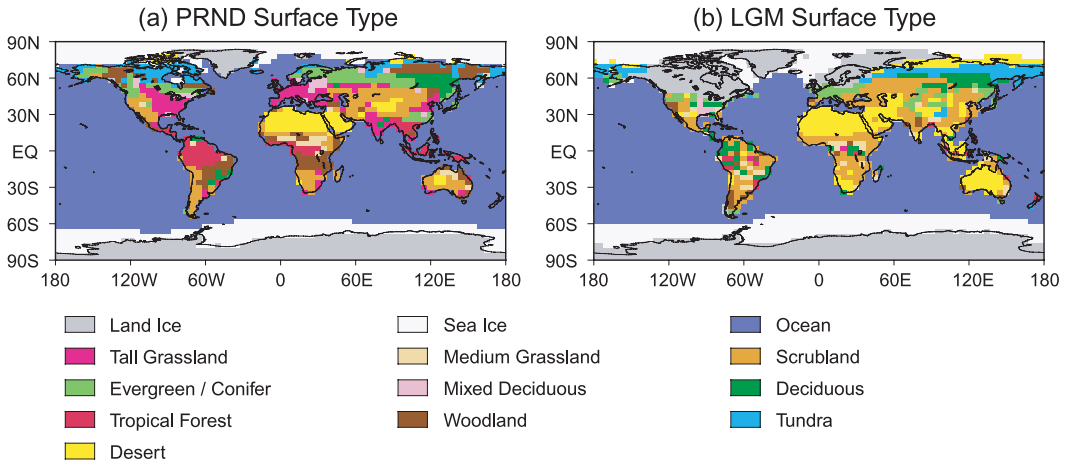

FIG. 1. Simulated land surface types during (a) the present day and (b) the LGM period.

least 10 out of 20 Peltier grid cells within one GCM grid box report ice sheet (Jiang et al. 2003). To get the LGM topography, the differences in elevation between the LGM and the present day from Peltier (2004) are added to the default present-day boundary data used by the IAP9L-AGCM (Jiang 2008). About the coastline, we define a GCM box as an ocean (land) grid cell if the calculated elevation is below (above) zero, following the approach used by Jiang et al. (2003).

The LGM SSTs over open water are calculated using the LGM ocean Q flux, which is obtained based on the energy balance between the predicted net atmosphere-to-ocean heat flux and the water heat content within the oceanic mixed layer derived from the Climate: Long-Range Investigation Mapping and Prediction (CLIMAP) LGM SSTs (CLIMAP Project Members 1981). Following Manabe and Broccoli (1985), the depth of the mixed layer ocean at the LGM is assumed to be the same as that in present day. The ocean model does not simulate sea ice; the monthly sea ice climatology from CLIMAP is used in simulations.

The equilibrium vegetation model BIOME3 (Haxeltine and Prentice 1996) was used to simulate the LGM land surface. The present-day vegetation in the BIOME3 is driven by the observed meteorological fields compiled by Leemans and Cramer (1991). Following the approach of Harrison et al. (1998), the climatic differences between the LGM and the present day simulated by the IAP9L-AGCM were added to the observed climate in the BIOME3 to simulate the LGM vegetation (Jiang 2008). The simulated distribution of the LGM vegetation was then used to replace the original surface types in the IAP9L-AGCM to simulate the new LGM climate. We repeated such routine several times until the predicted vegetation types showed small differences between the sequential iterations.

Figure 1b shows the predicted land cover at the LGM by the IAP9L-AGCM–BIOME3 coupling (Jiang 2008). Relative to present day (PRND; Fig. 1a), the area of deserts was predicted to increase largely during the glacial period. Over the tropical regions, the present-day rain forests over northern South America, central Africa, and Southeast Asia were predicted to be deciduous forests, scrubland, and even deserts at the LGM. In mid-latitudes, the present-day arid and semiarid areas over central Asia, South Africa, and Australia were found to expand during the LGM. At high latitudes in the NH, the present-day tundra over northern Siberia was simulated to be replaced by deserts. On a global scale, the total area of dust sources (including desert, scrubland, and short grassland) was predicted to increase by 82% at the LGM relative to present day.

e. *Numerical experiments*

For the purposes of this work, the following five main numerical experiments are performed (Table 1):

1) PRND: Simulation of present-day climate and dust cycle. Climate is one-way coupled with the dust cycle. Predicted present-day meteorological fields are used to simulate dust, but the radiative effects of dust are not fed back into the GCM climate. The concentration of atmospheric CO_2 is set to 345 ppmv.
2) LGM: Simulation of the LGM climate and dust cycle. The LGM climate (including vegetation) is simulated as described in the last section. Climate is one way coupled with the dust cycle. Predicted LGM meteorological fields are used to simulate LGM dust, but the radiative effects of dust are not fed back into the GCM climate. The concentration of atmospheric CO_2 is set to 200 ppmv.

TABLE 1. Summary of simulations.

Expt	Dust transport	Dust radiative effects (DRE) in the GCM climate
PRND	Present-day dust cycle with present-day climate	No DRE
LGM	LGM dust cycle with LGM climate	No DRE
LGM.DST	LGM dust cycle with LGM climate	SW+LW DRE with SSA = $1.0 \times \omega$
LGM.DST.SW	LGM dust cycle with LGM climate	SW only DRE with SSA = $1.0 \times \omega$
LGM.DST.HSSA	LGM dust cycle with LGM climate	SW+LW DRE with SSA = $1.1 \times \omega$

3) LGM.DST: Simulation of the LGM climate and dust cycle with the two-way dust–climate interactions. While the predicted LGM climate is used to drive the dust simulation, the SW and LW radiative effects of simulated dust particles are fed back into the GCM to influence the LGM climate.
4) LGM.DST.SW: This simulation is the same as LGM.DST, except that only the SW effect of dust is allowed to feed back into the LGM climate simulation.
5) LGM.DST.HSSA: This simulation is the same as LGM.DST that considers both the SW and LW radiative effects of dust, except that dust SSA is assumed to be higher by 10% in this simulation than in LGM.DST. The maximum SSA in this sensitivity run is set to 1.0.

The differences between LGM and PRND show the changes in climate between the LGM and present day. The differences between LGM.DST and LGM represent the climate responses to dust forcing at the LGM. Since the simulated climatic effect of dust depends on the consideration of dust LW radiative effect and the assumed dust SSA, we assess the sensitivity of the LGM temperature responses to LW RF and SSA of dust by performing LGM.DST.SW and LGM.DST.HSSA. The SSA of dust in LGM.DST is calculated based on the refractive indices from Woodward (2001) and is 0.89 at 0.55 μm over the Sahara Desert (Yue et al. 2010). The SSA over North Africa becomes 0.98 in LGM.DST.HSSA, close to the maximum values from observations (Forster et al. 2007).

Each of these five experiments is integrated for 50 yr. The model results averaged over the final 30 yr are analyzed and presented in the following sections. The Student's t test is used to calculate the statistical significance of the model results, and only the differences that exceed the 95% confidence level are discussed.

3. Simulation of dust climatology at the LGM

a. The simulated LGM climate

Figure 2a shows the predicted differences in surface air temperature (SAT) between simulations LGM and PRND. Relative to the present day, a widespread LGM cooling is predicted in mid to high latitudes in both hemispheres, with a maximum cooling exceeding 15 K located over the ice sheets between 60° and 80°N. The cooling over continents is generally larger than that over the oceans because of the higher heat capacity of the oceans. Globally, the terrestrial SAT is lower by 5.4 K at the LGM relative to present day. The averaged SAT over oceans (including sea ice) exhibits a cooling of 2.8 K. The SATs over the tropical Pacific in both hemispheres at the LGM are even warmer than those in present day because we use CLIMAP SST as initial conditions in climate simulations. Relative to present-day SSTs, the CLIMAP-reconstructed LGM SSTs show cooling of about 3°C in the tropical Atlantic but little or no cooling in the tropical Pacific (Jansen et al. 2007). As a result, the simulated weak LGM warming over the tropical Pacific might be some small variations/noises from model simulations.

The pattern of our predicted LGM cooling generally agrees with the reconstructions from paleogeologic and paleobiologic records (e.g., Rostek et al. 1993; Peyron et al. 1998; Sonzogni et al. 1998; Farrera et al. 1999; Tarasov et al. 2000) and resembles the ensemble means from the first and second phases of the Paleoclimate Modelling Intercomparison Project (PMIP1, PMIP2) simulations (Braconnot et al. 2007). On a global scale, the predicted annual-mean SAT is lowered by 3.7 K at the LGM as compared to present-day climate. This value is within the estimates of −3.3 to −4.7 K by models from PMIP1 and −3.6 to −5.7 K from PMIP2 (Braconnot et al. 2007).

The predicted differences in precipitation between simulations LGM and PRND are shown in Fig. 2b. Relative to present day, precipitation shows reductions over a large fraction of the continents. The largest reduction is predicted over South Asia, where heavy monsoon rainfall exists in present day. The expansion of ice sheets at the LGM leads to a decrease in global sea level and hence an increase in area of the desert in South Asia (Fig. 1b). Precipitation is also predicted to increase over the tropical oceans, especially over the tropical Pacific, because of the warmer-than-today SSTs in this region, as suggested by the CLIMAP reconstructions (Jiang 2008). The spatial pattern of changes in precipitation

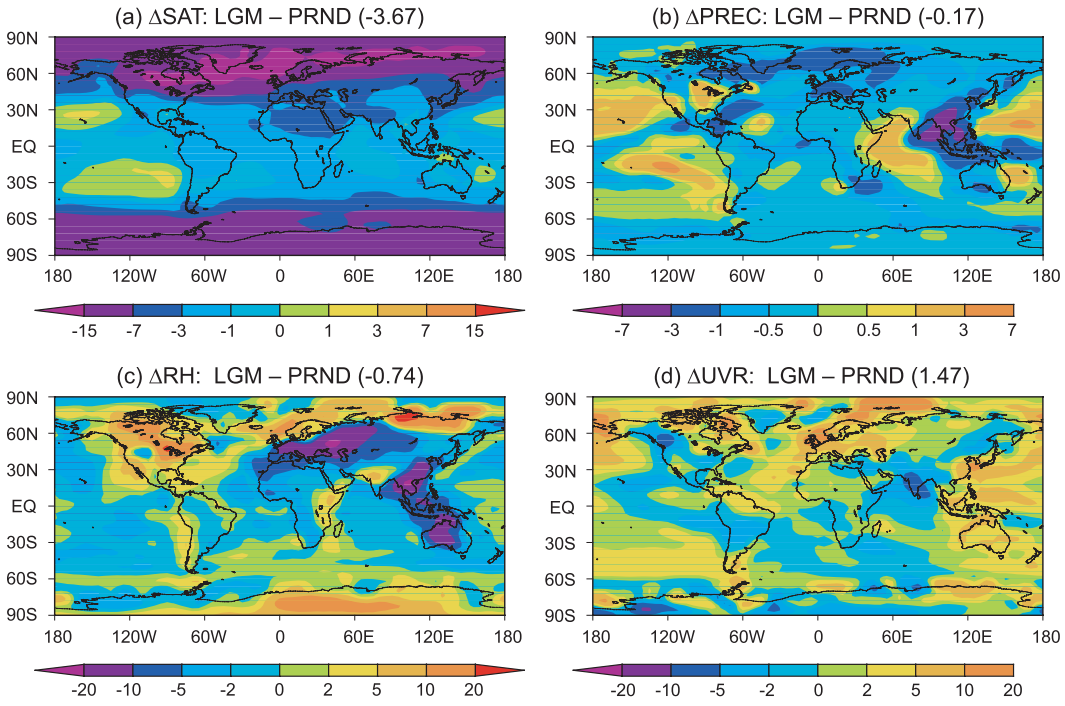

FIG. 2. Differences in predicted annual-mean (a) SAT (K), (b) precipitation (mm day^{-1}), (c) surface RH (%), and (d) UVR (cm s^{-1}) between the LGM and present-day climate. The globally averaged differences are indicated in parentheses. Results from the significance test are not shown in this figure because almost all the grid cells pass the 95% confidence level.

at the LGM simulated by the IAP9L-AGCM (Fig. 2b) is similar to that found in the ensemble mean of PMIP1 and PMIP2 simulations (Braconnot et al. 2007), with reductions in precipitation exceeding 1 mm day^{-1} predicted over South Asia, the equatorial Pacific, and high latitudes in the NH and increases in precipitation exceeding 0.5 mm day^{-1} over the western Indian Ocean and the subtropical Pacific. On a global- and annual-mean basis, a reduction of precipitation of 0.17 mm day^{-1} is predicted in LGM relative to present day.

Figures 2c and 2d show the changes in surface humidity and wind friction velocity (UVR), respectively, at the LGM relative to present day. On a global scale, the annual-mean RH at the surface is predicted to be lower by 0.74% during the glacial period. Relative humidity is predicted to be reduced significantly over Eurasia, Southeast Asia, and Australia (Fig. 2c) because of the differences in land surface between the LGM and present day (Fig. 1). The wind friction velocity intensifies over these dry regions (Fig. 2d). The glacial global-mean UVR is larger by 1.47 cm s^{-1} than the present-day value.

b. The simulated LGM dust

Figure 3 shows the predicted annual-mean dust emission in present day and LGM climate. Dust mobilization is more active during the LGM than in present day, with enhanced dust uplift over the Sahara Desert, Taklimakan Desert, Australia desert, and South Africa. Relative to present day, additional dust sources exist over Southeast Asia, eastern Europe, the West Siberian Plain, and the North Siberia Lowland at the LGM. Our predicted global and annual dust emission during the LGM is 2.3 times as large as that in present day, which is comparable to the estimates of 3.0 times by Mahowald et al. (1999), 2.2 times by Werner et al. (2002), and 2.4 times by Takemura et al. (2009).

The increase in dust emission during the LGM is attributed to two major factors. The first is the expansion of dust sources, since the exposure of continental shelves by the lowered sea level leads to the formation of new deserts along coastlines (such as the deserts over Southeast Asia and northwestern Australia; Fig. 1b) (Harrison et al. 2001), the long-term fine-grained outwash deposition along the margins of the NH ice sheets results in deserts at high latitudes (Harrison et al. 2001), and the aridity and low concentration of atmospheric CO_2 lead to the degeneration of vegetation and expansion of deserts (Mahowald et al. 1999). The second factor is the meteorological parameters (MPs) at the LGM. Both the dry surface air (Fig. 2c) and strong surface wind (Fig. 2d) facilitate large dust mobilization at the LGM [Eq. (1)].

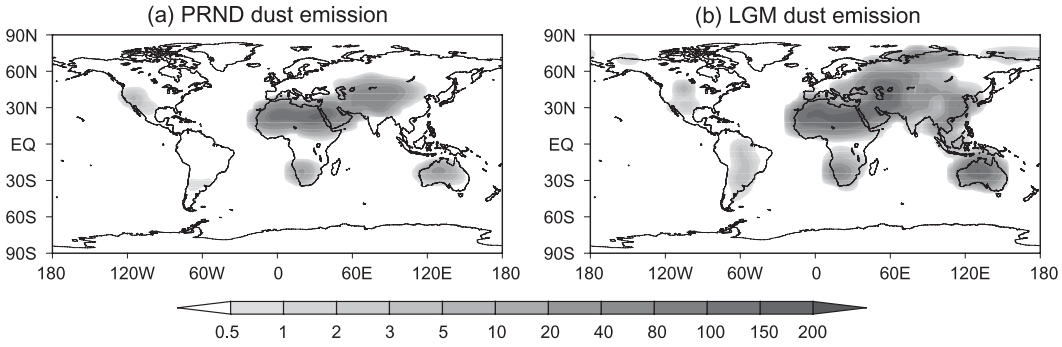

FIG. 3. Predicted annual-mean dust emission (g m^{-2} yr^{-1}) during (a) the present day and (b) the LGM period.

To quantify the roles of the two factors in the LGM dust uplift, we perform two sensitivity studies: "LGM MPs & current sources" and "current MPs & LGM sources." Global dust budgets from these two sensitivity runs and the simulations PRND and LGM are presented in Table 2. In simulation PRND (current MPs & current sources), the model predicts an annual total dust emission of 1966 Tg. The simulation LGM MPs & current sources obtains a dust emission of 2599 Tg yr^{-1}, indicating that the LGM meteorological condition alone increases dust emission by 633 Tg yr^{-1}. The simulation current MPs & LGM sources predicts an annual-mean dust emission of 2820 Tg yr^{-1}, indicating that the source expansion alone leads to an increase of 854 Tg yr^{-1} in dust uplift during the LGM. Considering both the LGM dust sources and the LGM MPs (simulation LGM), the model predicts a dust emission of 4579 Tg yr^{-1}, which is much higher than the other three cases. Our conclusions thus differ from those of Werner et al. (2002), who did not obtain large differences in total dust emission over expanded (LGM − PRND) dust sources when using either present-day or LGM MPs.

Table 3 compares the predicted dust budget at six latitudinal belts for both present day and the LGM. The increases in emission and burden between present day and the LGM are not spatially uniform. The largest percentage increases occur at the high latitudes in the NH, where dust emission, deposition, and column burden increase by factors of about 100, 10, and 10, respectively, relative to the present-day values. The largest absolute increases in dust mass are predicted over the tropical and subtropical regions in the NH. In the Southern Hemisphere (SH), the largest increase in dust mass occurs in the middle latitudes because of the expansion of the Australia desert and the dust sources in South Africa. In Antarctica, although there is no dust emission in both present day and the LGM, dust deposition and burden exhibit large increases at the LGM, reflecting the increase in emissions in the SH and the longer lifetime of dust particles as a result of the weakened hydrological cycle during the LGM (Yung et al. 1996). It should be noted that, because of the warm biases in CLIMAP LGM SSTs over the tropical Pacific, our simulation may overestimate precipitation (or wet deposition of dust) and hence underestimate dust concentrations there.

Table 4 shows simulated seasonal-mean emission and global burden of dust in present day and the LGM. The present-day global dust emission reaches a maximum in boreal summer, owing to the largest dust emission over the Sahara Desert in this season (Yue et al. 2009). The minimum dust uplift is found in boreal winter; the emission in winter is 26% of the value in summer. The seasonal variation of dust in the LGM is similar to that in present day, with maximum and minimum emissions in boreal summer and winter, respectively. However, the LGM dust emission in winter is 44% of that in summer, which can be attributed to the enhanced LGM dust emission in the SH.

Our predicted LGM dust is evaluated using dust deposition data from the Dust Indicators and Records of Terrestrial and Marine Paleoenvironments (DIRTMAP)

TABLE 2. Simulated dust budget in different experiments.

	PRND (current MPs & current sources)	LGM MPs & current sources	Current MPs & LGM sources	LGM (LGM MPs & LGM sources)
Uplift (Tg yr^{-1})	1966	2599	2820	4579
Dry (Tg yr^{-1})	1328	1799	1891	3155
Wet (Tg yr^{-1})	638	803	929	1424
Burden (Tg)	28.2	40.1	39.6	67.2
Lifetime (days)	5.2	5.6	5.1	5.4

TABLE 3. Comparisons of the predicted present-day and LGM dust emission (Tg yr^{-1}), deposition (Tg yr^{-1}), and burden (Tg) over different latitudes.

	Emission			Deposition			Burden		
	PRND	LGM	Ratio	PRND	LGM	Ratio	PRND	LGM	Ratio
61°–90°N	0.8	75	97.1	20	200	10.3	0.3	3.0	9.5
31°–60°N	500	1409	2.8	584	1383	2.4	7.0	19.7	2.8
0°–30°N	1316	2226	1.7	1138	1921	1.7	16.7	28.5	1.7
0°–30°S	105	754	7.2	162	783	4.8	3.3	12.4	3.8
31°–60°S	3	36	11.4	35	233	6.7	0.5	2.7	5.9
61°–90°S	0	0	—	0.6	3.7	5.9	0	0.1	3.2

(Mahowald et al. 1999; Kohfeld and Harrison 2001). The dataset is composed of the geologic records obtained from ice cores, marine sediments, and loess deposits. Most sites have both the present-day and LGM deposition data. Since the comparison of the simulated present-day dust deposition with measurements has been presented in Yue et al. (2009), we evaluate here the simulated deposition of dust during the LGM.

Figure 4 shows the distribution of the 147 DIRTMAP sites that have data on the LGM dust deposition. Over the Atlantic and Indian Oceans, the sites are mostly located in the tropical regions. Over the Pacific Ocean, most sites are in the midlatitudes in both hemispheres. Over Antarctica and Greenland, dust deposition values at the LGM were obtained from ice core records. The datasets over central China were derived from the loess sequences of the Chinese Loess Plateau.

The predicted annual-mean dust deposition at the LGM is compared with DIRTMAP data in Fig. 5. On a global scale, the logarithmic correlation coefficient between the observed and predicted LGM dust deposition is 0.72. Over the Atlantic, predicted dust deposition values at 27 out of the 29 sites are within a factor of 5 of the observations, indicating that the model predicts reasonable LGM dust emissions and concentrations over North Africa. Over the Indian Ocean, deposition rates at 20 out of 25 sites are within a factor of 5 of the observed values. The reconstructed LGM deposition over the Pacific Ocean ranges from 0.4 to 4600 Tg m^{-2} yr^{-1}. The model can predict reasonable medium values at most sites over the Pacific Ocean, but it does not perform well at the sites with large deposition values. In Antarctica, although the observed dust deposition during the LGM is about 10–20 times as large as the present-day value (Petit et al. 1990; Mahowald et al. 1999), the absolute value of deposition is very small. The model captures such features of deposition at the Antarctic sites.

The model has biases in simulating dust deposition over Greenland and central China. The model overestimates the deposition by a factor of 2–47 over Greenland, which may result from the representation of meridional winds in the GCM that overestimate the transport of dust from the mid to high latitudes. The model underestimates dust deposition in central China. Similar low bias also exists in present-day simulation of dust in this region (Yue et al. 2009). The reason is that although the model simulates dust particles with radii ranging from 0.1 to 10.0 μm, most loess samples contain particles of much larger size (e.g., Zhao et al. 2008).

4. Direct radiative forcing of dust at the LGM

a. Dust optical thickness

Simulated seasonal-mean dust optical thicknesses (DOTs) at 0.55 μm at the LGM are presented in Fig. 6. The global-mean DOT is predicted to be a maximum in boreal summer, similar to the prediction in present-day climate (Yue et al. 2010). However, while the maximum DOT is located over the Sahara Desert in present day, the highest DOT at the LGM is found over central Asia where Turan Plain now exists. The extreme aridity and gustiness over central Asia (Figs. 2c and 2d) contribute to the formation of this maximum DOT at the LGM. The DOT in the SH exhibits different seasonal variation; it reaches maximum and minimum in boreal winter and summer, respectively. Predicted global- and annual-mean DOT is 0.077 μm at the LGM, which is 2.4 times as large as the present-day value (Yue et al. 2010). A similar ratio of 2.8 was reported by Claquin et al. (2003), although they predicted a much higher absolute LGM DOT of 0.14.

TABLE 4. Simulated seasonal variation of global dust emission and burden (Tg) in present day and the LGM.

	MAM	JJA	SON	DJF
Current climate				
Total uplift	635.3	790.4	332.6	208.1
Burden	33.5	44.8	21.9	12.5
LGM climate				
Total uplift	1214.3	1681.3	951.0	732.2
Burden	59.0	104.5	60.4	44.7

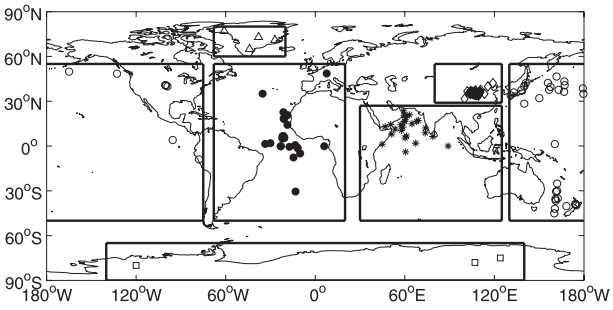

FIG. 4. Distribution of the 147 DIRTMAP sites that have the LGM datasets. Solid circles denote sites over the Atlantic and in Europe; triangles denote sites in Greenland; asterisks denote sites over the Indian Ocean; diamonds denote sites in China; empty circles denote sites over the Pacific Ocean, North America, and South America; squares denote sites in Antarctica; and diamonds denote sites in the South Pacific.

b. Dust direct radiative forcing

The dust RF at the LGM is calculated with a ''double radiation call'' method as described in Woodward (2001) and Yue et al. (2010). The simulated SW and LW RFs of dust aerosol are shown in Fig. 7. At the TOA, the strong absorption by dust particles leads to positive SW forcing values over the regions with high surface albedo, such as deserts and ice sheets in the NH (Fig. 7a). A similar pattern was also reported by Takemura et al. (2009), although different refractive indices were used in their simulation. At the surface, dust aerosol greatly reduces the downward solar radiation over the source regions. The large negative SW forcing exceeding 10 W m^{-2} is predicted over the Sahara Desert and central Asia. The LW forcings of dust aerosol are positive at both the TOA and surface, with larger values at the surface than at the TOA. While the maximum LW heating is as high as +21.0 W m^{-2} at the surface, the maximum value at the TOA is +5.3 W m^{-2}. The presence of mineral dust aerosol in the LGM atmosphere is estimated to exert global- and annual-mean SW and LW RFs of −0.58 and +0.68 W m^{-2} at the TOA and −4.69 and +1.70 W m^{-2} at the surface, respectively.

It should be mentioned that there are large uncertainties in previously estimated RFs by the LGM dust. Claquin et al. (2003) reported that the net LGM dust RF at TOA is −3.2 W m^{-2} for externally mixed dust (i.e., quartz and hematite present as separate grains, transported independently, yielding the lowest SW absorption) and −2.2 W m^{-2} for internally mixed dust (i.e., quartz coated with hematite, yielding the highest SW absorption). Takemura et al. (2009) estimated that the SW and LW direct RFs of dust aerosol at the LGM are −0.24 and +0.22 W m^{-2} at the TOA, respectively. The uncertainties among different studies arise from the differences in prescribed or calculated aerosol concentrations, vertical profiles of dust, estimated dust optical properties, and surface albedo.

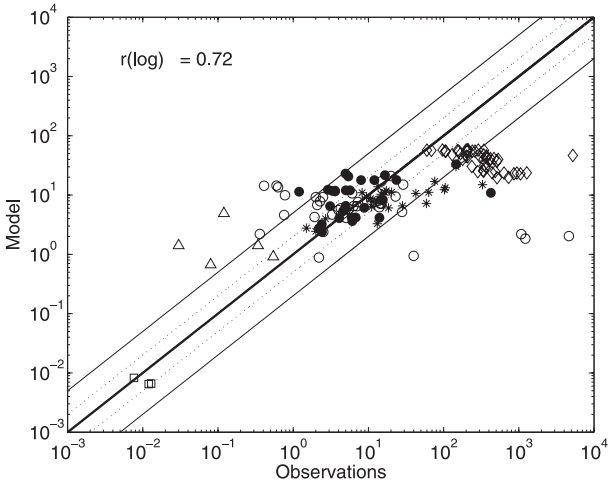

FIG. 5. Comparison of the predicted dust deposition with the LGM proxy values at the DIRTMAP sites (g m^{-2} yr^{-1}). Bold solid diagonal means simulations and observations are in perfect agreement. Dashed lines indicate that the ratios of simulated value to observation are 2.0 or 0.5. Thin solid lines indicate that the ratios of simulated value to observation are 5.0 or 0.2. The scales of the coordinates are logarithmic. Symbols are as in Fig. 4.

The seasonal variation of predicted dust RF is shown in Table 5. The maximum RFs of dust aerosol appear in June–August (JJA), when dust concentrations are the highest in a year (Table 4). The surface forcings are about the same in March–May (MAM) and September–November (SON), corresponding to about the same dust burdens in these two seasons. The SW forcing at the TOA shows stronger cooling in SON than in MAM, which is caused by the difference in seasonal variation in the two hemispheres. In MAM, dust emission is more active in the NH, where a large area is covered with ice sheets in the high latitudes. The high surface albedo in the high latitudes in the NH leads to SW warming at the TOA by dust aerosol (figures not shown). In the SH, dust concentrations are high during SON (Fig. 6); however, no ice sheets exist in the mid to low latitudes, resulting in SW cooling by dust at the TOA (figures not shown). This also explains why the TOA SW cooling in December–February (DJF) is stronger than that in MAM, although the global dust burden in DJF is lower than that in MAM (Table 4).

5. Climatic effect of dust at the LGM

Figure 8a shows the annual-mean SAT responses to the net (SW+LW) radiative effects of dust at the LGM. The SW+LW RF of the LGM dust leads to a widespread cooling exceeding 0.3 K over the tropical oceans (30°S–30°N), with a regional-mean cooling of 0.85 K over the tropical Atlantic (10°–30°N, 60°–15°W). Such strong cooling in SST induced by dust helps to explain in

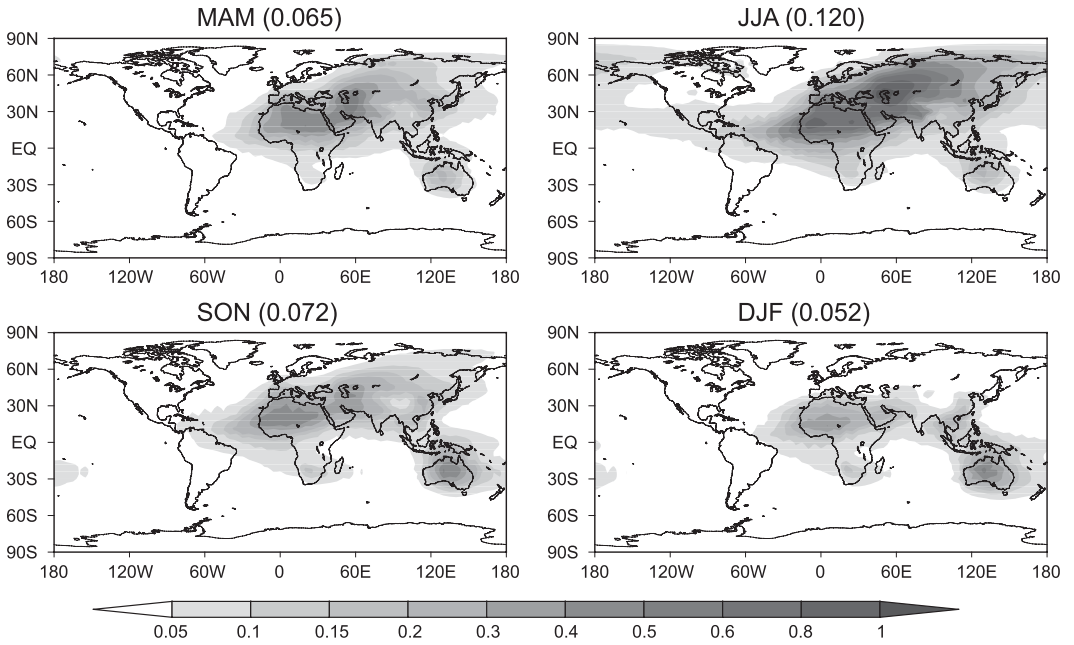

FIG. 6. Seasonal variations of the predicted LGM dust optical thickness at 0.55 μm. The global and seasonal averages are shown in parentheses.

part the reconstructed cooling in this region (Guilderson et al. 1994; Wolff et al. 1998). The SATs are predicted to increase over North Africa, central Asia, and North America in the presence of LGM dust, as a result of the combined effects of dust LW heating and SW absorption over high-albedo ice and snow (Overpeck et al. 1996). On a global scale, dust aerosol is predicted to lead to an annual-mean SAT cooling of 0.18 K, which accounts for only 5% of the global-mean LGM cooling relative to present day (Fig. 2a). The net radiative effect of dust even leads to a general warming over the continents at mid and high latitudes in the NH. Our result indicates that, with the assumed optical properties of dust in our LGM.DST simulation, the consideration of dust direct radiative forcing in our climate model cannot improve the global-mean underestimate of the severe cold during the LGM.

The dust-induced cooling over the tropical oceans does not show strong seasonal variation. Over the continents, the warming is stronger in JJA than in DJF (Figs. 8b and 8c) because of the net positive TOA forcing in JJA (Table 5). As a result, the global-mean SAT shows a smaller reduction by the LGM dust in JJA than in DJF, although dust concentrations are the highest in JJA.

The changes in annual-mean precipitation by the LGM dust are shown in Fig. 9a. The dust-induced cooling over the oceans inhibits evaporation, leading to a decrease in global precipitation. The maximum reduction in precipitation occurs over the Atlantic Ocean, where dust particles from the Sahara Desert have high concentrations. Precipitation over central Africa is predicted to increase because the absorption of radiation by dust reverses the local diabatic heating dominated by longwave cooling and leads to an anomalous ascent (Menon et al. 2002; Miller et al. 2004). The pattern of the responses in precipitation to the LGM dust RF resembles that of the responses to present-day dust forcing (Yue et al. 2010), except that the magnitude of the responses during the LGM is much larger than that in present day.

On an annual- and global-mean basis, the LGM dust induces a reduction in precipitation by 0.06 mm day^{-1}. Over the oceans, the reduction in precipitation is predicted to be larger in JJA than in DJF as a result of the largest net surface RF cooling in JJA (Table 5). The reduction in precipitation by the LGM dust contributes to the aridity during the glacial period (Fig. 2b). The changes in precipitation can feed back into the dust cycle; the reduced wet deposition increases the burden of dust aerosol, especially the burden of small particles (Yue et al. 2010), which contributes to the strong dust-induced surface cooling at the LGM.

6. Uncertainties in simulated climatic effect of the LGM dust

We further quantify the uncertainties in simulated LGM climatic responses to dust aerosol with the two additional sensitivity experiments LGM.DST.SW and LGM.DST.HSSA. Predicted differences in simulated

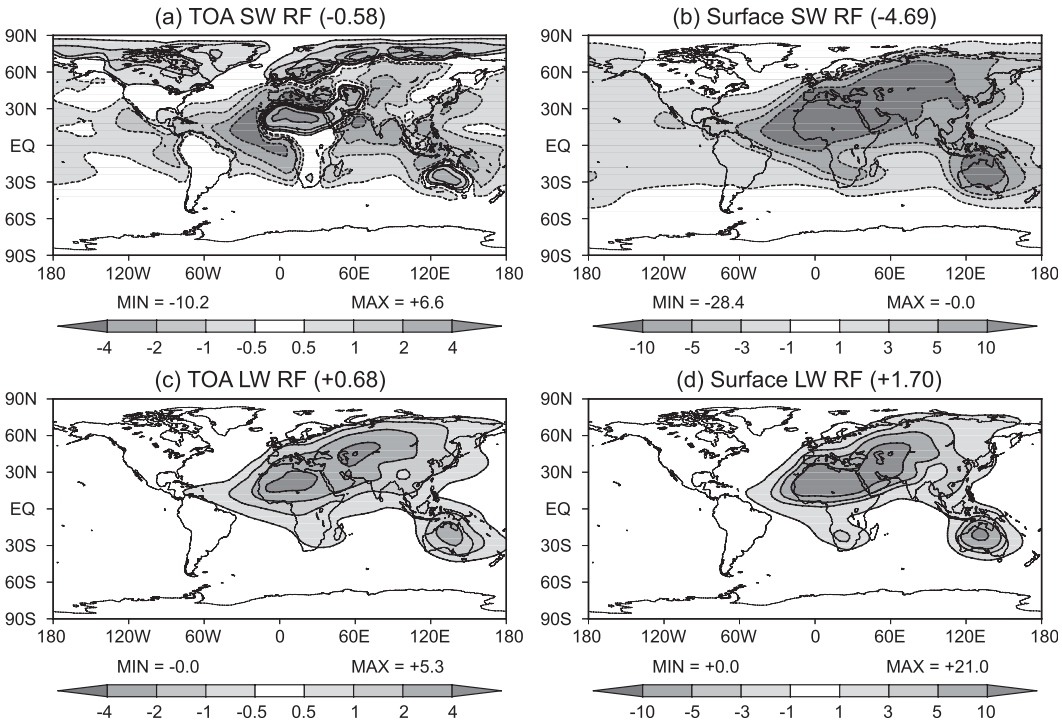

FIG. 7. Predicted annual-mean all-sky dust RF (W m^{-2}) at the LGM: (a) SW RF at the TOA, (b) SW RF at the surface, (c) LW RF at the TOA, and (d) LW RF at the surface. The global-mean RF is indicated in parentheses above each panel. Solid and dashed lines are positive and negative contours, respectively. Positive values indicate increases of downward radiation.

annual-mean SAT between LGM.DST.SW and LGM are shown in Fig. 10a. The omission of dust LW absorption in LGM.DST.SW leads to a global cooling of 0.37 K by LGM dust, which is 0.19 K cooler than that simulated with both SW and LW RFs of dust in LGM.DST (Fig. 8a). An average cooling of 0.42 K in SAT is predicted over the tropical oceans, with the regional-mean value reaching −1.08 K over the tropical Atlantic. Over North Africa, central Asia, and eastern Europe, the dust-induced warming in Fig. 8a is replaced by cooling in Fig. 10a, indicating that the warming over these regions is caused by the LW heating of dust. However, the predicted warming over North America in Fig. 8a still exists in Fig. 10a, suggesting that the SW absorption by the LGM dust over the high-albedo ice sheets is the dominant factor that leads to the warming over North America.

Predicted differences in simulated annual-mean SAT between LGM.DST.HSSA and LGM are shown in Fig. 10b. The high SSA in LGM.DST.HSSA reduces the SW absorption by dust significantly; a strong global-mean cooling of 0.63 K is predicted in LGM.DST.HSSA even with both the SW and LW effects of the LGM dust. The global-mean cooling of 0.63 K accounts for 17% of the global cooling during the glacial period (Fig. 2a). Regionally, a maximum cooling of 1.2 K is predicted over East Asia. Over the tropical oceans, a widespread reduction exceeding 0.8 K in SAT is predicted over the Atlantic and Indian Oceans.

The predictions in LGM.DST.HSSA can be further explained by RF values. With the increase in the SSA by 10% in LGM.DST.HSSA, the LGM dust leads to stronger SW cooling at the TOA (Fig. 11a) and weaker cooling at the surface (Fig. 11b), as compared to Figs. 7a and 7b, respectively. These changes in dust RF are consistent with the results of Liao and Seinfeld (1998) [the increase in SSA here is equivalent to the reduction in the imaginary part of refractive index of dust in Liao and Seinfeld (1998)]. As a result, the SW RF of dust aerosol in LGM.DST.HSSA exerts large cooling at the TOA (Fig. 11a), even over the high-albedo surfaces, such as

TABLE 5. Simulated seasonal variation of the LGM dust RF (W m^{-2}). Positive values indicate increases of downward radiation.

	MAM	JJA	SON	DJF
TOA				
SW	−0.38	−0.75	−0.63	−0.57
LW	+0.58	+1.18	+0.56	+0.39
Surface				
SW	−4.00	−7.39	−4.05	−3.31
LW	+1.52	+2.68	+1.45	+1.13

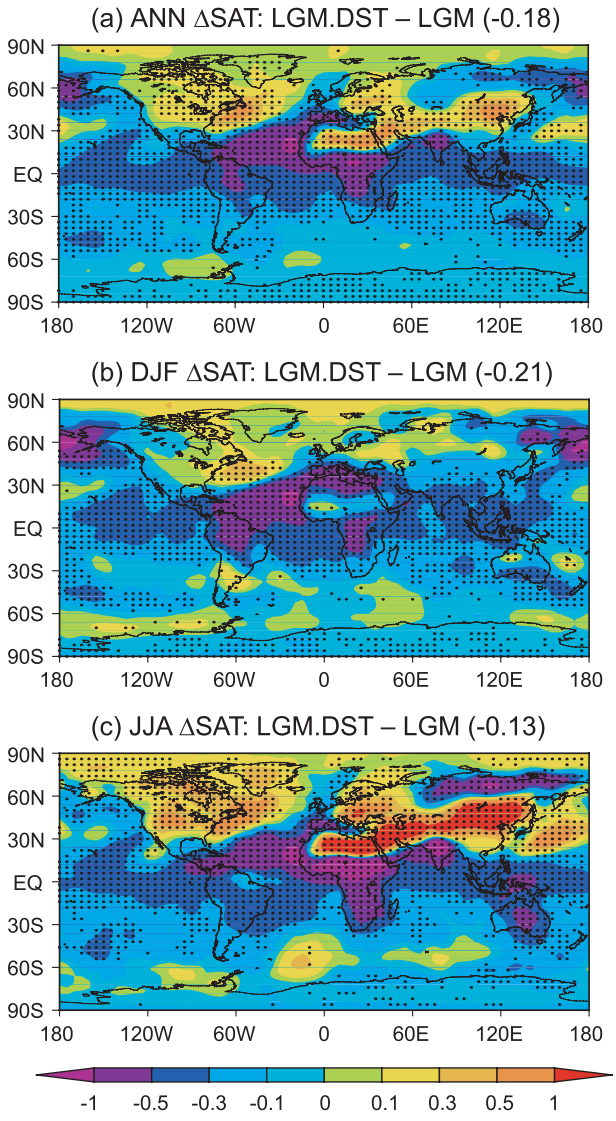

FIG. 8. Predicted changes in the (a) annual, (b) DJF, and (c) JJA mean SAT (K) at the LGM induced by SW+LW RF of dust aerosol. The differences that pass the 95% significance level are denoted with dots. The globally averaged changes are indicated in brackets.

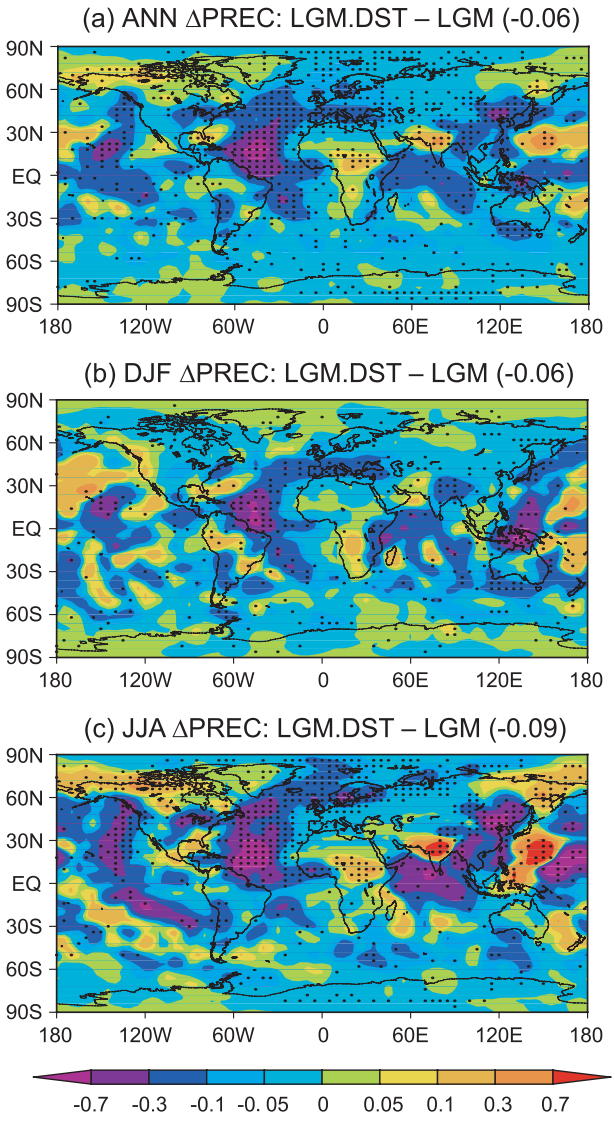

FIG. 9. As in Fig. 8, but for mean precipitation (mm day^{-1}).

deserts and ice sheets. On a global scale, the LGM dust with the increased SSA of 0.98 exerts SW RF of -1.79 W m^{-2} at the TOA and -3.27 W m^{-2} at the surface. The net RF of the LGM dust at the TOA becomes a negative value of -1.11 W m^{-2} in this case, which is close to the value estimated by Mahowald et al. (2006b).

7. Conclusions

We used a global dust model embedded in a GCM to examine the climatic responses to the direct RF of dust aerosol at the LGM. The climate model is asynchronously coupled with the vegetation model BIOME3 to obtain the glacial vegetation distribution. The predicted LGM vegetation shows that the cooling and aridity during the glacial period lead to a widespread decrease in vegetation and an expansion of dust sources, which favor stronger dust mobilization together with intensified glacial wind. As a result, the global dust emission at the LGM is predicted to be 2.3 times as large as the present-day value. The percentage increase of dust uplift at the LGM is greatest at high latitudes in the NH and smallest over the tropical and subtropical regions in the same hemisphere.

Based on the predicted dust climatology at the LGM, the DOT and RF of dust are estimated. On an annual- and global-mean basis, the simulated DOT is 0.077 at 0.55 μm, which is about 2.4 times as large as the present-day value. At the surface, dust aerosol leads to a negative SW RF globally, with the maximum cooling located over

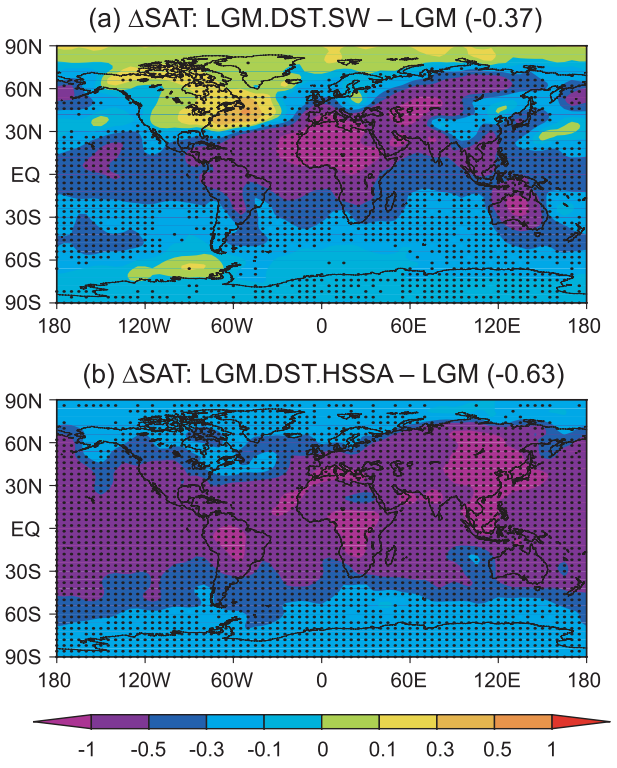

FIG. 10. Predicted changes in the annual-mean SAT (K) in (a) LGM.DST.SW and (b) LGM.DST.HSSA experiments relative to simulation LGM. The differences that pass the 95% significance level are denoted with dots. The globally averaged changes are indicated in brackets.

North Africa. At the TOA, strong absorption of dust particles leads to positive SW forcing over high-albedo surfaces, such as deserts and ice sheets. The predicted global- and annual-mean SW RF of LGM dust is -4.69 W m^{-2} at the surface and -0.58 W m^{-2} at the TOA, and the LW RF is $+1.70$ W m^{-2} at the surface and $+0.68$ W m^{-2} at the TOA.

With both the SW and LW radiative effects, the dust-induced change in annual- and global-mean SAT at the LGM is predicted to be -0.18 K. An average cooling of 0.85 K is predicted over the tropical Atlantic Ocean. Over North Africa and central Asia, SAT is predicted to increase by about 1.0 K in boreal summer but decrease by about 0.2 K in boreal winter. The cooling by the LGM dust predicted in this control simulation is smaller overall than that estimated in previous studies (e.g., Harvey 1988; Mahowald et al. 2006b; Bar-Or et al. 2008).

The dust-induced cooling over the oceans inhibits evaporation, leading to a reduction in precipitation, especially over the tropical Atlantic and Indian Oceans. The reduction in precipitation is larger over the oceans than over the continents. The global- and annual-mean precipitation is predicted to be reduced by 0.06 mm day^{-1} in the presence of the LGM dust. As a result, dust direct radiative effect enhances the aridity at the LGM.

We further examine the uncertainties in estimating the climatic effect of the LGM dust that may arise from the consideration of dust LW and/or SW absorption. The absence of dust LW radiative effect is predicted to further decrease the LGM global- and annual-mean SAT by 0.19 K. When the SSA of Saharan dust at 0.55 μm increases from 0.89 in simulation LGM.DST to 0.98 in LGM.DST.HSSA, the dust-induced LGM annual- and global-mean surface cooling increases from 0.18 to 0.63 K even with both SW and LW radiative effects of the aerosol, indicating that simulated climatic effect of the LGM dust is very sensitive to the assumed SSA of dust. In these two sensitivity experiments, the dust-induced cooling in SAT over the tropical oceans increase to 0.42 and 0.72 K, respectively.

Although there are uncertainties, our study shows that the direct radiative effects of dust play an important role in influencing the cooling and aridity at the LGM.

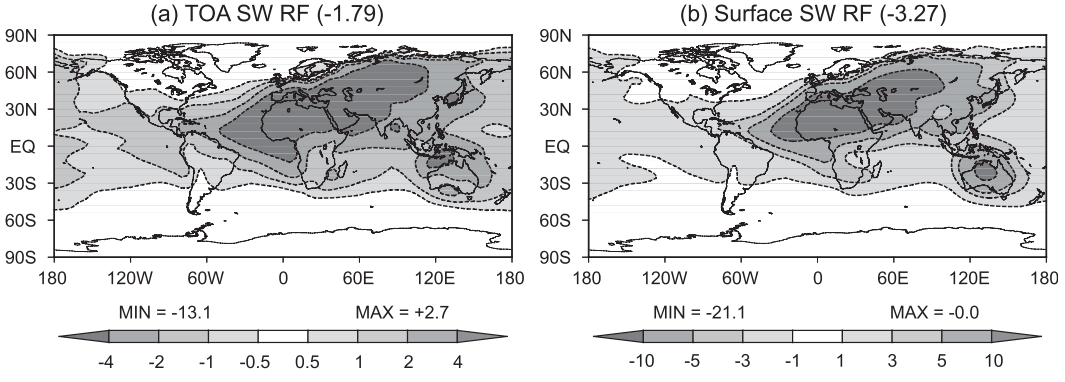

FIG. 11. Predicted annual-mean all-sky dust SW RF (W m^{-2}) at the (a) TOA and (b) surface during the LGM period in the sensitivity simulation LGM.DST.HSSA. The global-mean RF is indicated in parentheses above each panel. Solid and dashed lines are positive and negative contours, respectively. Positive values indicate increases of downward radiation.

Considering that the CLIMAP SSTs used in our simulations may have some warm biases over tropical oceans and may lead to larger precipitation (or higher wet deposition of dust), we may the underestimate direct effects of dust in this work. It also should be noted that the indirect effect of dust is not considered here. Takemura et al. (2009) reported that the magnitude of indirect RF of the LGM dust is larger than that of its direct RF. Future research needs to include the indirect effect of dust in LGM climate simulations to better understand the roles of dust at the LGM.

Acknowledgments. This research was jointly supported by the Key Project of the Chinese Academy of Sciences under Grants KZCX2-YW-Q1-02, KZCX2-YW-Q11-03, KZCX2-YW-205, and KZCX2-YW-219, and the National Natural Science Foundation of China under Grants 40631005, 40825016, and 90711004.

REFERENCES

Andersen, K. K., A. Armengaud, and C. Genthon, 1998: Atmospheric dust under glacial and interglacial conditions. *Geophys. Res. Lett.,* **25,** 2281–2284.

Ballantyne, A. P., M. Lavine, T. J. Crowley, J. Liu, and P. B. Baker, 2005: Meta-analysis of tropical surface temperatures during the Last Glacial Maximum. *Geophys. Res. Lett.,* **32,** L05712, doi:10.1029/2004GL021217.

Barnola, J. M., D. Raynaud, Y. S. Korotkevich, and C. Lorius, 1987: Vostok ice core provides 160,000-year record of atmospheric CO_2. *Nature,* **329,** 408–414.

Bar-Or, R., C. Erlick, and H. Gildor, 2008: The role of dust in glacial–interglacial cycles. *Quat. Sci. Rev.,* **27,** 201–208.

Berger, A. L., 1978: Long-term variations of daily insolation and quaternary climatic changes. *J. Atmos. Sci.,* **35,** 2362–2367.

Braconnot, P., and Coauthors, 2007: Results of PMIP2 coupled simulations of the mid-Holocene and Last Glacial Maximum – Part 1: Experiments and large-scale features. *Climate Past,* **3,** 261–277.

Briegleb, B. P., 1992: Delta-Eddington approximation for solar radiation in the NCAR community climate model. *J. Geophys. Res.,* **97,** 7603–7612.

Carlson, T. N., and S. G. Benjamin, 1980: Radiative heating rates for Saharan dust. *J. Atmos. Sci.,* **37,** 193–213.

Claquin, T., and Coauthors, 2003: Radiative forcing of climate by ice-age atmospheric dust. *Climate Dyn.,* **20,** 193–202.

CLIMAP Project Members, 1981: Seasonal reconstructions of the earth's surface at the Last Glacial Maximum. Geological Society of America Tech. Rep. MC-36, 18 pp.

de Rooij, W. A., and C. C. A. H. van der Stap, 1984: Expansion of Mie scattering matrices in generalized spherical functions. *Astron. Astrophys.,* **131,** 237–248.

Farrera, I., and Coauthors, 1999: Tropical climates at the Last Glacial Maximum: A new synthesis of terrestrial palaeoclimate data. I. Vegetation, lake levels and geochemistry. *Climate Dyn.,* **15,** 823–856.

Forster, P., and Coauthors, 2007: Changes in atmospheric constituents and in radiative forcing. *Climate Change 2007: The Physical Science Basis,* S. Solomon et al., Eds., Cambridge University Press, 129–234.

Genthon, C., 1992: Simulations of desert dust and sea-salt aerosols in Antarctica with a general circulation model of the atmosphere. *Tellus,* **44B,** 371–389.

Guilderson, T. P., R. G. Fairbanks, and J. L. Rubenstone, 1994: Tropical temperature variations since 20,000 years ago: Modulating interhemispheric climate change. *Science,* **263,** 663–665.

Hansen, J., A. Lacis, D. Rind, G. Russell, P. Stone, I. Fung, R. Ruedy, and J. Lerner, 1984: Climate sensitivity: Analysis of feedback mechanisms. *Climate Processes and Climate Sensitivity, Geophys. Monogr.,* Vol. 29, Amer. Geophys. Union, 130–163.

Harrison, S. P., and Coauthors, 1998: Intercomparison of simulated global vegetation distributions in response to 6 kyr BP orbital forcing. *J. Climate,* **11,** 2721–2742.

——, K. E. Kohfeld, C. Roelandt, and T. Claquin, 2001: The role of dust in climate changes today, at the last glacial maximum and in the future. *Earth Sci. Rev.,* **54,** 43–80.

Harvey, D., 1988: Climatic impact of ice-age aerosols. *Nature,* **334,** 333–335.

Haxeltine, A., and I. C. Prentice, 1996: BIOME3: An equilibrium terrestrial biosphere model based on ecophysiological constraints, resource availability, and competition among plant functional types. *Global Biogeochem. Cycles,* **10,** 693–709.

Jansen, E. J., and Coauthors, 2007: Palaeoclimate. *Climate Change 2007: The Physical Science Basis,* S. Solomon et al. Eds., Cambridge University Press, 433–497.

Jiang, D., 2008: Vegetation and soil feedbacks at the Last Glacial Maximum. *Palaeogeogr. Palaeoclimatol. Palaeoecol.,* **268,** 39–46.

——, H. Wang, H. Drange, and X. Lang, 2003: Last Glacial Maximum over China: Sensitivities of climate to paleovegetation and Tibetan ice sheet. *J. Geophys. Res.,* **108,** 4102, doi:10.1029/2002JD002167.

——, ——, Z. Ding, X. Lang, and H. Drange, 2005: Modeling the middle Pliocene climate with a global atmospheric general circulation model. *J. Geophys. Res.,* **110,** D14107, doi:10.1029/2004JD005639.

Joussaume, S., 1993: Paleoclimatic tracers — An investigation using an atmospheric general circulation model under ice age conditions. 1. Desert dust. *J. Geophys. Res.,* **98,** 2767–2805.

Ju, L. X., H. J. Wang, and D. B. Jiang, 2007: Simulation of the Last Glacial Maximum climate over East Asia with a regional climate model nested in a general circulation model. *Palaeogeogr. Palaeoclimatol. Palaeoecol.,* **248,** 376–390.

Kohfeld, K. E., and S. P. Harrison, 2000: How well can we simulate past climates? Evaluating the models using global palaeoenvironmental datasets. *Quat. Sci. Rev.,* **19,** 321–346.

——, and ——, 2001: DIRTMAP: The geological record of dust. *Earth Sci. Rev.,* **54,** 81–114.

Krinner, G., O. Boucher, and Y. Balkanski, 2006: Ice-free glacial northern Asia due to dust deposition on snow. *Climate Dyn.,* **27,** 613–625.

Leemans, R., and W. P. Cramer, 1991: The IIASA climate database for mean monthly values of temperature, precipitation, and cloudiness on a terrestrial grid. International Institute for Applied Systems Analysis Research Rep. RR-91-18, 68 pp.

Levitus, S., J. I. Antonov, T. P. Boyer, and C. Stephens, 2000: Warming of the world ocean. *Science,* **287,** 2225–2229.

Liang, X., 1996: Description of a nine-level grid point atmospheric general circulation model. *Adv. Atmos. Sci.,* **13,** 269–298.

Liao, H., and J. H. Seinfeld, 1998: Radiative forcing by mineral dust aerosols: Sensitivity to key variables. *J. Geophys. Res.,* **103,** 31 637–31 645.

Lohmann, U., and K. Diehl, 2006: Sensitivity studies of the importance of dust ice nuclei for the indirect aerosol effect on stratiform mixed-phase clouds. *J. Atmos. Sci.,* **63,** 968–982.

Lunt, D. J., and P. J. Valdes, 2002: Dust deposition and provenance at the Last Glacial Maximum and present day. *Geophys. Res. Lett.,* **29,** 2085, doi:10.1029/2002GL015656.

Mahowald, N., K. Kohfeld, M. Hansson, Y. Balkanski, S. Harrison, I. Prentice, M. Schulz, and H. Rodhe, 1999: Dust sources and deposition during the Last Glacial Maximum and current climate: A comparison of model results with paleodata from ice cores and marine sediments. *J. Geophys. Res.,* **104,** 15 895–15 916.

——, D. R. Muhs, S. Levis, P. J. Rasch, M. Yoshioka, C. S. Zender, and C. Luo, 2006a: Change in atmospheric mineral aerosols in response to climate: Last glacial period, preindustrial, modern, and doubled carbon dioxide climates. *J. Geophys. Res.,* **111,** D10202, doi:10.1029/2005JD006653.

——, M. Yoshioka, W. D. Collins, A. J. Conley, D. W. Fillmore, and D. B. Coleman, 2006b: Climate response and radiative forcing from mineral aerosols during the Last Glacial Maximum, pre-industrial, current and doubled-carbon dioxide climates. *Geophys. Res. Lett.,* **33,** L20705, doi:10.1029/2006GL026126.

Manabe, S., and A. J. Broccoli, 1985: The influence of continental ice sheets on the climate of an ice age. *J. Geophys. Res.,* **90,** 2167–2190.

Menon, S., J. Hansen, L. Nazarenko, and Y. F. Luo, 2002: Climate effects of black carbon aerosols in China and India. *Science,* **297,** 2250–2253.

Miller, R. L., and I. Tegen, 1998: Climate response to soil dust aerosols. *J. Climate,* **11,** 3247–3267.

——, ——, and J. Perlwitz, 2004: Surface radiative forcing by soil dust aerosols and the hydrologic cycle. *J. Geophys. Res.,* **109,** D04203, doi:10.1029/2003JD004085.

Mishchenko, M. I., J. M. Dlugach, E. G. Yanovitskij, and N. T. Zakharova, 1999: Bidirectional reflectance of flat, optically thick particulate layers: An efficient radiative transfer solution and applications to snow and soil surfaces. *J. Quant. Spectrosc. Radiat. Transfer,* **63,** 409–432.

Overpeck, J., D. Rind, A. Lacis, and R. Healy, 1996: Possible role of dust-induced regional warming in abrupt climate change during the last glacial period. *Nature,* **384,** 447–449.

Painter, T. H., A. P. Barrett, C. C. Landry, J. C. Neff, M. P. Cassidy, C. R. Lawrence, K. E. McBride, and G. L. Farmer, 2007: Impact of disturbed desert soils on duration of mountain snow cover. *Geophys. Res. Lett.,* **34,** L12502, doi:10.1029/2007GL030284.

Patrick, A., and R. C. Thunell, 1997: Tropical Pacific sea surface temperatures and upper water column thermal structure during the Last Glacial Maximum. *Paleoceanography,* **12,** 649–657.

Peltier, W. R., 2004: Global glacial isostasy and the surface of the ice-age earth: The ICE-5G (VM2) model and GRACE. *Annu. Rev. Earth Planet. Sci.,* **32,** 111–149.

——, and S. Marshall, 1995: Coupled energy-balance/ice-sheet model simulations of the glacial cycle: A possible connection between terminations and terrigenous dust. *J. Geophys. Res.,* **100,** 14 269–14 289.

Petit, J. R., L. Mounier, J. Jouzel, Y. S. Korotkevich, V. I. Kotlyakov, and C. Lorius, 1990: Palaeoclimatological and chronological implications of the Vostok core dust record. *Nature,* **343,** 56–58.

Peyron, O., J. Guiot, R. Cheddadi, P. Tarasov, M. Reille, J.-L. de Beaulieu, S. Bottema, and V. Andrieu, 1998: Climatic reconstruction in Europe for 18,000 yr B.P. from pollen data. *Quat. Res.,* **49,** 183–196.

Prospero, J. M., and Coauthors, 1996: Atmospheric deposition of nutrients to the North Atlantic basin. *Biogeochemistry,* **35,** 27–73.

Ramanathan, V., and P. Downey, 1986: A nonisothermal emissivity and absorptivity formulation for water vapor. *J. Geophys. Res.,* **91,** 8649–8666.

Rostek, F., G. Ruhlandt, F. C. Bassinot, P. J. Muller, L. D. Labeyrie, Y. Lancelot, and E. Bard, 1993: Reconstructing sea-surface temperature and salinity using $\delta^{18}O$ and alkenone records. *Nature,* **364,** 319–321.

Sassen, K., 2002: Indirect climate forcing over the western US from Asian dust storms. *Geophys. Res. Lett.,* **29,** 1465, doi:10.1029/2001GL014051.

Schneider von Deimling, T., A. Ganopolski, H. Held, and S. Rahmstorf, 2006: How cold was the Last Glacial Maximum? *Geophys. Res. Lett.,* **33,** L14709, doi:10.1029/2006GL026484.

Sonzogni, C., E. Bard, and F. Roster, 1998: Tropical sea-surface temperatures during the last glacial period: A view based on alkenones in Indian Ocean sediments. *Quat. Sci. Rev.,* **17,** 1185–1201.

Takemura, T., M. Egashira, K. Matsuzawa, H. Ichijo, R. O'Ishi, and A. Abe-Ouchi, 2009: A simulation of the global distribution and radiative forcing of soil dust aerosols at the Last Glacial Maximum. *Atmos. Chem. Phys.,* **9,** 3061–3073.

Tarasov, P. E., and Coauthors, 2000: Last Glacial Maximum biomes reconstructed from pollen and plant macrofossil data from northern Eurasia. *J. Biogeogr.,* **27,** 609–620.

Wang, H. J., 1999: Role of vegetation and soil in the Holocene megathermal climate over China. *J. Geophys. Res.,* **104,** 9361–9367.

——, 2002: The mid-Holocene climate simulated by a grid-point AGCM coupled with a biome model. *Adv. Atmos. Sci.,* **19,** 205–218.

Wang, Z. F., H. Ueda, and M. Y. Huang, 2000: A deflation module for use in modeling long-range transport of yellow sand over East Asia. *J. Geophys. Res.,* **105,** 26 947–26 959.

Watson, A. J., D. C. E. Bakker, A. J. Ridgwell, P. W. Boyd, and C. S. Law, 2000: Effect of iron supply on southern ocean CO_2 uptake and implications for glacial atmospheric CO_2. *Nature,* **407,** 730–733.

Werner, M., I. Tegen, S. P. Harrison, K. E. Kohfeld, I. C. Prentice, Y. Balkanski, H. Rodhe, and C. Roelandt, 2002: Seasonal and interannual variability of the mineral dust cycle under present and glacial climate conditions. *J. Geophys. Res.,* **107,** 4744, doi:10.1029/2002JD002365.

Wolff, T., S. Mulitza, H. Arz, J. Patzold, and G. Wefer, 1998: Oxygen isotopes versus CLIMAP (18 ka) temperatures: A comparison from the tropical Atlantic. *Geology,* **26,** 675–678.

Woodward, S., 2001: Modeling the atmospheric life cycle and radiative impact of mineral dust in the Hadley Centre climate model. *J. Geophys. Res.,* **106,** 18 155–18 166.

Yue, X., and H. Wang, 2009: The application of the CCM3/NCAR radiation scheme in IAP-AGCM (in Chinese). *Chin. J. Atmos. Sci.,* **33,** 16–28.

——, ——, Z. Wang, and K. Fan, 2009: Simulation of dust aerosol radiative feedback using the Global Transport Model of Dust: 1. Dust cycle and validation. *J. Geophys. Res.,* **114,** D10202, doi:10.1029/2008JD010995.

——, ——, H. Liao, and K. Fan, 2010: Simulation of dust aerosol radiative feedback using the GMOD: 2. Dust-climate interactions. *J. Geophys. Res.,* **115,** D04201, doi:10.1029/2009JD012063.

Yung, Y. L., T. Lee, C. H. Wang, and Y. T. Shieh, 1996: Dust: A diagnostic of the hydrologic cycle during the Last Glacial Maximum. *Science,* **271,** 962–963.

Zeng, Q.-C., X.-H. Zhang, X.-Z. Liang, C.-G. Yuan, and S.-F. Chen, 1989: Documentation of IAP (Institute of Atmospheric Physics) two-level atmospheric general circulation model. Stony Brook University Tech. Rep. DOE/ER/60314-H1, 387 pp.

Zhang, X., 1990: Dynamical framework of IAP nine-level atmospheric general circulation model. *Adv. Atmos. Sci.,* **7,** 67–77.

Zhang, Z., H. Wang, Z. Guo, and D. Jiang, 2007a: Impacts of tectonic changes on the reorganization of the Cenozoic paleoclimatic patterns in China. *Earth Planet. Sci. Lett.,* **257,** 622–634.

——, ——, ——, and ——, 2007b: What triggers the transition of palaeoenvironmental patterns in China, the Tibetan Plateau uplift or the Paratethys Sea retreat? *Palaeogeogr. Palaeoclimatol. Palaeoecol.,* **245,** 317–331.

Zhao, J., H. Lu, F. Mei, X. Zhang, Y. Li, and L. Wen, 2008: Simulation of grain size distribution of Xining loess accumulation (in Chinese). *Arid Land Geogr.,* **31,** 31–37.